On the adequacy of OH* as heat release marker for hydrogen–air flames

Francesco G Schiavone, Andrea Aniello, Eleonore Riber, Thierry Schuller, Davide Laera

On the adequacy of OH* as heat release marker for hydrogen-air flames

Francesco G. Schiavone[a], Andrea Aniello[b], Eleonore Riber[c], Thierry Schuller[b,d], Davide Laera[a,*]

[a]*Department of Mechanics, Mathematics and Management, Polytechnic University of Bari, Via Orabona 4, Bari 70125, Italy*
[b]*Institut de Mécanique des Fluides de Toulouse, IMFT, Université de Toulouse, CNRS, Toulouse 31400, France*
[c]*CERFACS, 42 avenue Gaspard Coriolis, Toulouse 31057, France*
[d]*Institut Universitaire de France (IUF)*

Abstract

The correlation between the distributions of OH* and heat release rate (HRR) is numerically investigated for laminar and turbulent hydrogen-air flames. First, laminar premixed one-dimensional flames are considered, observing a peak shift between OH* and HRR regardless of the equivalence ratio or OH* sub-mechanism. Nevertheless, OH* and HRR well correlate for methane-hydrogen fuel mixtures, suggesting that the reasons for such peak shift are to be searched in the hydrogen flame intrinsic properties. In particular, the H-radical is pivotal, given its different role in the main OH* formation and HRR reaction pathways. The chain-branching nature of hydrogen oxidation enhances the formation of H-radical pool, leading to higher OH* production in the post-flame region, while HRR peaks upstream, being linked to the consumption of HO_2 generated by the recombination reactions of back-diffused H-radicals. Methane oxidation, instead, is chain-terminating, hence H-consuming, releasing heat and preventing the radical pool formation in the post-flame zone. Similar analyses are then performed for strained counterflow diffusion hydrogen-air flames, where the OH* distribution shows to be, at least for strain levels not close to extinction, an adequate HRR marker. Indeed, differently from premixed flames, HRR is here found to be dominated by H direct consumption on the fuel side. The observations made for laminar one-dimensional flames are confirmed by Large Eddy Simulations (LES) of three-dimensional turbulent hydrogen-air diffusion and partially premixed flames, stabilized in the HYLON injector at IMFT laboratory. When compared with the experimental OH* field, LES-computed HRR correctly retrieves OH* position in the diffusion flame, while a mismatch in the axial direction is observed between the two distributions for the lifted partially premixed flame. An overall good match, instead, is observed between measured and LES-computed OH* fields, emphasizing the importance of including OH* kinetics to accurately compare simulations and experiments of multi-regime hydrogen-air flames.

Keywords: OH* chemiluminescence; Heat release rate; Premixed flames; Diffusion flames; Hydrogen combustion

* Corresponding author.
Preprint submitted to Proceedings of the Combustion Institute

1. Introduction

The distribution of heat release rate (HRR) is crucial to analyzing and predicting flame structure and its dynamics [1, 2]. Being difficult to simultaneously measure several species and temperature, HRR direct measurements are impractical. The correlation of other measurable quantities with HRR has therefore been the topic of many investigations [3–5] and chemiluminescence, i.e., the spontaneous light emission from excited chemical species in flames, is often used as a tracer of HRR [3, 6].

A good correlation between CH^*, OH^* and $CO_2{}^*$ chemiluminescent intensities and HRR is generally observed in steady hydrocarbon flames [2]. For pure methane (CH_4) flames, the peak-to-peak distance between OH^* intensity and HRR profiles is smaller than the spatial resolution of most optical chemiluminescence measurement devices [7]. Hu et al. [8], adopting the methodology described in [4], investigated the quantitative relation between HRR and chemiluminescence and found a strong linear correlation of HRR with OH^* at fixed equivalence ratio, making light radiation of this radical well appropriate to detect the flame front [6]. A correspondence between OH^* intensity and HRR distributions has been found also for methane-hydrogen blends of various compositions [9]. For hydrogen (H_2)-air flames, instead, the OH^* emission is weaker than for hydrocarbon fuels [10]. Moreover, the distance between the peaks of OH^* and HRR is rather wide [11], raising doubts on the adequacy of OH^* chemiluminescence as HRR marker when pure H_2 is burnt and leading to the study of alternative HRR markers [5]. Despite these previous works, to the best of our knowledge, a systematic investigation of the mechanisms leading to the production of OH^* both in H_2 and CH_4-H_2 flames and its relation with HRR is still lacking.

Numerical simulations complement experiments to gain an understanding. Several kinetic mechanisms have been developed to describe OH^* formation and consumption both for hydrocarbon [7] and hydrogen [12, 13] flames. Still, given the diverse kinetic descriptions provided by each scheme, their comparison is required to understand the impact of the different OH^* chemical pathways on the main characteristics of the OH^* distribution and to assess their applicability in numerical flow simulations.

Aiming to fill these gaps, the first part of this work investigates laminar premixed H_2-air flames for different equivalence ratios, examining pathways leading to OH^* and HRR peaks to understand their intrications. Results obtained with OH^* sub-schemes by Kathrotia et al. [12] and Konnov [13] are compared. Differences between H_2 and CH_4 flames are also investigated. Furthermore, simulations of laminar counterflow diffusion flames are performed to evaluate the differences with premixed flames and assess the impact of flame stretch on the OH^* and HRR distributions. Finally, measurements in turbulent three-dimensional H_2-air flames, stabilized above a coaxial dual-swirl injector [14], are compared with results of Large Eddy Simulations (LES) including OH^* kinetics. Thus, the capability of numerical OH^* to correlate better with experiments than numerical HRR is investigated.

2. Description of OH^* kinetics

In hydrogen flames, the OH^* formation and consumption relies on three elementary reactions [15]:

$$\mathrm{H + O + M \rightleftharpoons OH^* + M} \quad \text{(R1)}$$

$$\mathrm{OH^* \longrightarrow OH} + h\nu \quad \text{(R2)}$$

$$\mathrm{OH^* + M \rightleftharpoons OH + M} \quad \text{(R3)}$$

where $h\nu$ is the energy of the emitted photon. Below 2800 K, chemical excitation dominates thermal excitation and the three-body recombination reaction (R1) is considered to be the main OH^* formation path [16]. The other two represent the channels for unstable OH^* to transfer the excess energy and return to the ground state, either by emitting light in the radiative decay reaction (R2) or by the non-reactive collisional quenching reaction (R3) [12]. The former is at the basis of OH^* chemiluminescence, whose intensity is recorded experimentally. This study adopts the mechanism reported in Table 1, proposed by Kathrotia et

Table 1: OH^* sub-scheme for H_2-air combustion, based on Kathrotia et al. [12].

No.	Reaction	A	n	E_a
(A1)	$H + O + M \rightleftharpoons OH^* + M$	1.50E+13	0.0	5975
	With M = $[H_2]$ + 6.5$[H_2O]$ + 0.4$[O_2]$ + 0.4$[N_2]$			
(A2)	$OH^* \longrightarrow OH + h\nu$	1.45E+06	0.0	0
(A3a)	$OH^* + O_2 \rightleftharpoons OH + O_2$	2.10E+12	0.5	-483
(A3b)	$OH^* + H_2O \rightleftharpoons OH + H_2O$	5.93E+12	0.5	-863
(A3c)	$OH^* + H_2 \rightleftharpoons OH + H_2$	2.95E+12	0.5	-445
(A3d)	$OH^* + OH \rightleftharpoons OH + OH$	6.01E+12	0.5	-762
(A3e)	$OH^* + H \rightleftharpoons OH + H$	1.31E+12	0.5	-167
(A3f)	$OH^* + N_2 \rightleftharpoons OH + N_2$	1.08E+11	0.5	-1240

$k = AT^n \exp(-E_a/RT)$, units are cm^3 mol s cal K.

Table 2: OH^* sub-scheme for H_2-air combustion, based on Konnov [13].

No.	Reaction	A	n	E_a
(B1)	$H + O + M \rightleftharpoons OH^* + M$	1.50E+13	0.0	5970
	With M = $[H_2]$ + 6.5$[H_2O]$ + 0.4$[O_2]$ + 0.4$[N_2]$			
(B2)	$OH^* \longrightarrow OH + h\nu$	1.40E+06	0.0	0
(B3a)	$OH^* + O_2 \rightleftharpoons OH + O_2$	8.40E+11	0.5	-482
(B3b)	$OH^* + H_2O \rightleftharpoons OH + H_2O$	2.96E+12	0.5	-861
(B3c)	$OH^* + H_2 \rightleftharpoons OH + H_2$	3.54E+11	0.5	-444
(B3d)	$OH^* + OH \rightleftharpoons OH + OH$	1.50E+12	0.5	0
(B3e)	$OH^* + H \rightleftharpoons OH + H$	1.50E+12	0.5	0
(B3f)	$OH^* + N_2 \rightleftharpoons OH + N_2$	1.08E+11	0.5	-1238
(B3g)	$OH^* + O \rightleftharpoons OH + O$	1.50E+12	0.5	0
(B4)	$OH^* + H_2 \rightleftharpoons H_2O + H$	2.60E+12	0.5	-444
(B5)	$OH^* + O_2 \rightleftharpoons HO_2 + O$	1.01E+12	0.5	-482
(B6)	$OH^* + H_2O \rightleftharpoons H_2O_2 + H$	2.96E+12	0.5	-861

$k = AT^n \exp(-E_a/RT)$, units are cm^3 mol s cal K.

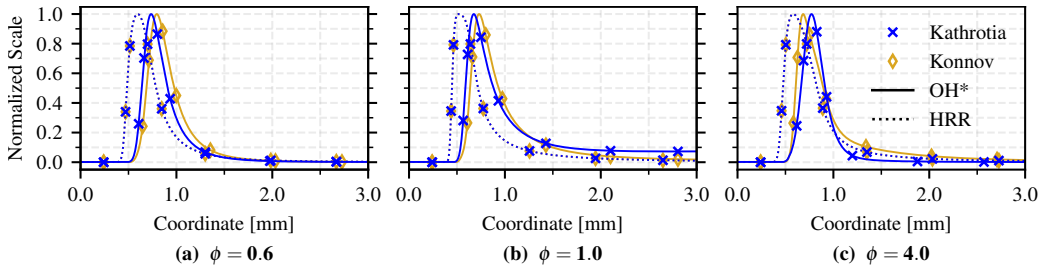

(a) $\phi = \mathbf{0.6}$ **(b)** $\phi = \mathbf{1.0}$ **(c)** $\phi = \mathbf{4.0}$

Fig. 1: HRR and OH* molar concentration (normalized by the maximum value) for lean (a), stoichiometric (b) and rich (c) H_2-air flames at T_u = 300 K and p = 1 atm. Comparison between Kathrotia (Table 1) and Konnov (Table 2) OH* sub-mechanisms.

al. [12] and widely used [15]. To assess the impact of the chosen sub-mechanism on the predicted OH* distribution, results obtained with the Kathrotia sub-scheme are compared with those from the sub-scheme by Konnov [13], reported in Table 2. Both OH* sub-schemes are based on the three reactions (R1) to (R3). The main differences are the rate constants' coefficients for reaction (R3) and the disregard in [12] of O as collision partner for reaction (B3g), as was proposed instead by Hidaka et al. [16]. Furthermore, Konnov [13] includes reactive quenching reactions (B4), (B5) and (B6), considering them to substantially contribute to the overall OH* collisional quenching.

When CH_4 is involved, OH* kinetics still relies on reactions (R1) to (R3), with CO_2, CO and CH_4 as additional collision partners. The main OH* formation path, however, is given by the following reaction [11]:

$$CH + O_2 \rightleftharpoons OH^* + CO \qquad (R4)$$

The rate coefficients reported in [17] are used in this work in reaction (R3), for the non-reactive quenching involving CO_2, CO and CH_4, and in reaction (R4). Collision efficiencies from [18] are added in reaction (R1) for CO_2 (1.5), CO (0.75) and CH_4 (3.0).

In all cases, the OH* sub-mechanism is simply added to the main reaction scheme describing fuel oxidation, since the relative change in the concentration of ground species due to its addition is negligible [19].

3. Laminar one-dimensional flames

Steady, one-dimensional, laminar H_2-air flames are computed with Cantera [20] to investigate the relation between the spatial distributions of OH* and HRR. These are compared with CH_4-H_2-air flames at variable H_2 content ranging from 10% to 90% by volume, and with pure CH_4-air flames taken as reference. One-dimensional flame simulations are performed with the multi-component transport model [21], including Soret effect, relevant for H_2 flames in low-velocity zones with temperature gradients [22]. Two detailed mechanisms, namely the San Diego (UCSD) [23] and the CRECK [24], are used to describe ground species oxidation. The former is adopted for studies of pure H_2-air flames, while the latter, involving hydrocarbons, is used when comparing H_2-air, CH_4-H_2-air and CH_4-air flames. The two schemes are compared for H_2-air flames in the Supplementary Material, showing negligible differences in the results. First, the impact of the sub-mechanism chosen for OH* kinetics is discussed to assess the robustness of the results and the conclusions presented in this study. Secondly, the reaction pathways leading to OH* and HRR distributions are investigated. Finally, H_2-air laminar diffusion flames are considered, to investigate the impact of stretch on OH* and HRR peak-to-peak distance. The analysis is further expanded by comparing the OH*-HRR relation in the different cases from a quantitative perspective.

3.1. Unstrained premixed flames

Unstrained premixed flames at an unburned mixture temperature T_u = 300 K and a pressure p = 1 atm are here considered. The impact of the different OH* sub-mechanisms on the spatial distributions of OH* is assessed in Fig. 1 for lean (a, ϕ = 0.6), stoichiometric (b, ϕ = 1.0), and rich (c, ϕ = 4.0) H_2-air mixtures. The different descriptions of collisional quenching induce only slight differences between the two sub-mechanisms in the OH* profiles. A consistent peak shift between OH* and HRR distributions, previously observed in [5] for lean flames, is confirmed also for stoichiometric and rich ones. This suggests that the reasons for the observed peak shift are not to be found in the OH* kinetics as such, but rather in the inherent properties of H_2 flames. The Kathrotia scheme is thus chosen in the following.

Pure H_2-air and CH_4-air flames are compared in Fig. 2. CH_4-H_2 blends with various H_2 contents are also considered, to investigate the different behaviors when modifying the fuel blend composition. The adequacy of OH* as HRR marker for the different cases is first characterized by considering the peak shift δ_{peak} between the two distributions (cross-marked black line), here normalized by the thermal flame thickness $\delta_L^0 = (T_b - T_u)/\max(dT/dx)$, where T_b is the temperature of the burned mixture. When CH_4 is present, the peak shift δ_{peak} remains almost constant and lower than 10% of δ_L^0, sustaining the adequacy of OH* as HRR marker for carbon-based fuels. For pure H_2, however, δ_{peak} suddenly rises to a value of about 50% of δ_L^0.

To explain this behavior, the most important reactions responsible for the position of OH* and HRR peaks are studied. For OH*, the reaction rates of the two main formation paths, namely reactions (R1) and (R4), are considered. For HRR, the heat released by

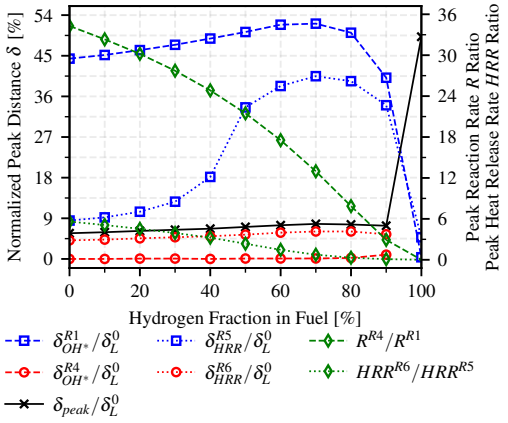

Fig. 2: Peak distances, normalized by δ^0_L, between OH* and total HRR (δ_{peak}), rate of reaction (R1) and OH* ($\delta^{R1}_{OH^*}$), rate of reaction (R4) and OH* ($\delta^{R4}_{OH^*}$), HRR of reaction (R5) and total HRR (δ^{R5}_{HRR}), HRR of reaction (R6) and total HRR (δ^{R6}_{HRR}) (left axis), and ratio of peak values of rates of reactions (R4) and (R1) (R^{R4}/R^{R1}), and of HRR of reactions (R6) and (R5) (HRR^{R6}/HRR^{R5}) (right axis), versus H_2 volume fraction in the CH_4+H_2 fuel mixture. Results obtained for $\phi = 1$, $T_u = 300$ K and $p = 1$ atm.

the following reactions is instead taken into account:

$$H + O_2 + M \rightleftharpoons HO_2 + M, \qquad (R5)$$

$$OH + CH_2O \rightleftharpoons HCO + H_2O. \qquad (R6)$$

In H_2-air flames, reaction (R5) describes the heat released by recombination and production of the hydroperoxyl radical (HO_2) [25, 26]. For CH_4-air flames, the exothermic reaction (R6) has a strong linear correlation with HRR and, therefore, the formyl radical (HCO) can be used as a marker [7, 8]. Figure 2 reports the ratios R^{R4}/R^{R1} between peak values of rates of reactions (R4) and (R1) (diamond-marked green dashed line), and HRR^{R6}/HRR^{R5} between heat released by reactions (R6) and (R5) (diamond-marked green dotted line) as a function of the H_2 content in the fuel mixture. Both ratios decrease almost linearly with increasing H_2 content, highlighting the growing importance of the H_2-related OH* and HRR pathways (i.e., reactions (R1) and (R5), respectively) compared to the CH_4 flames.

To outline the relation of these reactions with the peak location of either OH* or HRR, four characteristic distances are introduced: $\delta^{R1}_{OH^*}$ and $\delta^{R4}_{OH^*}$ are evaluated as the distances between the peak of OH* and the peaks of the rates of reactions (R1) and (R4), while δ^{R5}_{HRR} and δ^{R6}_{HRR} measure the distances between the peak of HRR and the peaks of heat released by reactions (R5) and (R6), respectively. The evolution versus H_2 content of these distances, normalized by δ^0_L, is also shown in Fig. 2. Differently from the ratios R^{R4}/R^{R1} and HRR^{R6}/HRR^{R5}, when CH_4 is present in the fuel mixture, $\delta^{R4}_{OH^*}$ and δ^{R6}_{HRR} (circle-marked red dashed and dotted lines, respectively) are relatively low ($\sim 0.05\delta^0_L$) and remain approximately constant, regardless of the relative concentration of H_2 and CH_4. Analogous curves for H_2-related reactions (R1), $\delta^{R1}_{OH^*}$ (square-marked dashed blue line), and (R5), δ^{R5}_{HRR} (square-marked dotted blue line), show that these peak distances increase at first, reaching a maximum for the 30% CH_4 + 70% H_2 (by volume) fuel blend, then decrease becoming almost zero for pure hydrogen. Therefore, these trends suggest that the H_2 content in the fuel mixture has a limited impact on the CH-driven OH* formation pathway of reaction (R4) and on the correlation between HCO and HRR via reaction (R6), while reactions (R1) and (R5), driven by the H-radical, are representative of the OH* and HRR peaks, respectively, only for pure H_2-air flames. This is coherent with the trend of δ_{peak} versus H_2 content, and with the analysis in Section 3.3.

To investigate the underlying reasons for these different behaviors, the flame structures for CH_4-air, CH_4-H_2-air (30% CH_4 + 70% H_2 fuel by volume) and H_2-air flames are compared in Fig. 3. From the asymptotic analysis standpoint, the structure of a premixed flame, apart from the upstream transport region, can be considered as two-layered, with a thin fuel consumption layer and a thicker downstream region where chemical equilibrium is approached [27]. In CH_4 flames (Fig. 3a), the threshold between the two layers is marked by the H-radical profile: in the downstream layer, H is produced (green-shaded zone) and supplied through back-diffusion to the fuel consumption layer (red-shaded zone). Observing the H-radical profile (dashed red line), this is also a H-consumption region, where CH_4 is depleted with H-radicals according to the following chain-terminating reaction [28]:

$$CH_4 + 2\,H + H_2O \rightleftharpoons CO + 4\,H_2 \qquad (R7)$$

limiting the H-radical upstream diffusion and pool generation. The so-produced secondary fuels H_2 and CO are then consumed in the downstream oxidation layer to obtain the final products H_2O and CO_2 [28].

For H_2 flames (Fig. 3c), instead, the asymptotic analysis is more difficult, given the chain-branching nature of the global fuel consumption reaction [29]:

$$O_2 + 3\,H_2 \rightleftharpoons 2\,H_2O + 2\,H \qquad (R8)$$

Nevertheless, H maintains a pivotal role, and downstream H-production (green-shaded zone) as well as upstream H-consumption (red-shaded zone) layers can still be identified [25]. The H-consumption layer corresponds to an upstream radical recombination region [26], coinciding with the maximum of the HO_2 profile (dash-dotted blue line), coherently with reaction (R5). Heat is mostly released in this zone, despite the moderate temperatures [25, 28]. Downstream, equilibrium is reached in a second, thicker radical recombination region, with the transition between the two occurring in a thin radical branching layer, near the H-profile peak [26].

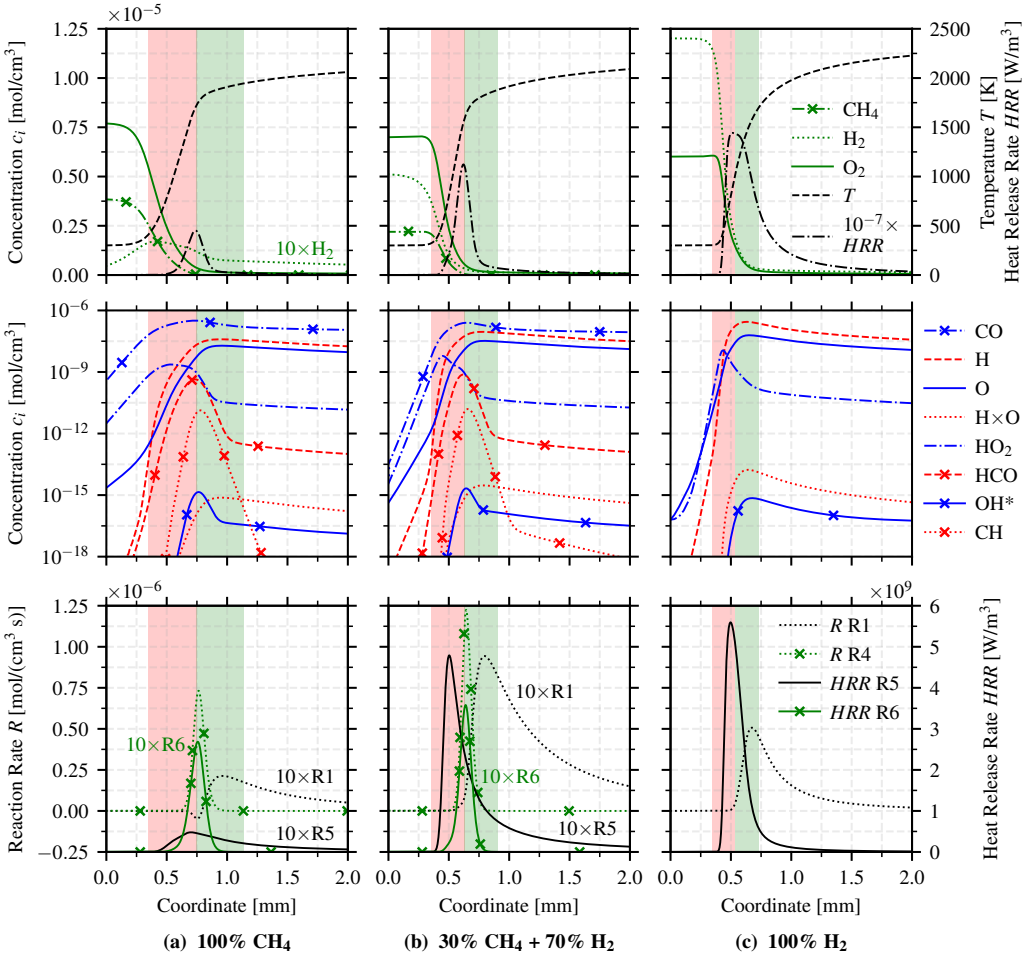

Fig. 3: Structures of stoichiometric CH_4-air (a), 30%CH_4+70%H_2-air (b) and H_2-air (c) flames at T_u = 300 K and p = 1 atm. Molar concentrations of fuel and oxidizer, temperature and heat release rate profiles (top), molar concentrations of selected minor species (middle), chemical rates and heat release rates of selected reactions (bottom). The red and green zones represent, respectively, the main H-consumption and production regions.

Figure 3 shows that, as observed in [19], the two-layered structure of the host flame is kept with OH*, which is produced in the fuel consumption layer, where it reaches the peak value, and then slowly decays to the equilibrium value in the downstream region. In the pure CH_4 flame (Fig. 3a), given the low availability of H, rapidly consumed via reaction (R7), the main production pathway of OH*, namely reaction (R4) (cross-marked dotted green line), peaks at the front of the inner layer, following its precursor CH (cross-marked dotted red line) together with HCO (cross-marked dashed red line), HRR position marker via reaction (R6), thus explaining why no significant peak shift is observed in this case. For the pure H_2 flame (Fig. 3c), instead, the OH* concentration profile (cross-marked solid blue line) follows those of the rate of reaction (R1) (dotted black line) and of the product of the concentrations of its reactants H and O (dotted red line), peaking at the back of the active reaction zone. On the other hand, HRR (dash-dotted black line) peaks at the front, given the strong exothermicity of reaction (R5) (solid black line) and the fast back-diffusion of H (dashed red line), leading to the observed peak shift. For the CH_4-H_2 fuel mixture (Fig. 3b), although the reduced CH_4 content facilitates the H-radical pool generation, the path provided by reaction (R4) remains by far the most important for OH* production. The highest HRR still occurs in the back high-temperature region of the active reaction zone, keeping the peak shift negligible.

3.2. Strained counterflow diffusion flames

Strained counterflow diffusion H_2-air flames are considered for varying global strain rate $a = (|u_F| + |u_O|)/d$, with u_F and u_O being the inlet velocities of fuel and oxidizer jets, respectively, and d the distance between the two injectors. The objective is to investigate the effect of strain rate on the OH* and HRR distributions.

Figure 4 shows that HRR exhibits a bimodal distribution for all strain rates. The two peaks are here referred to as HRR^F_{max}, on the fuel side, and HRR^O_{max}, on

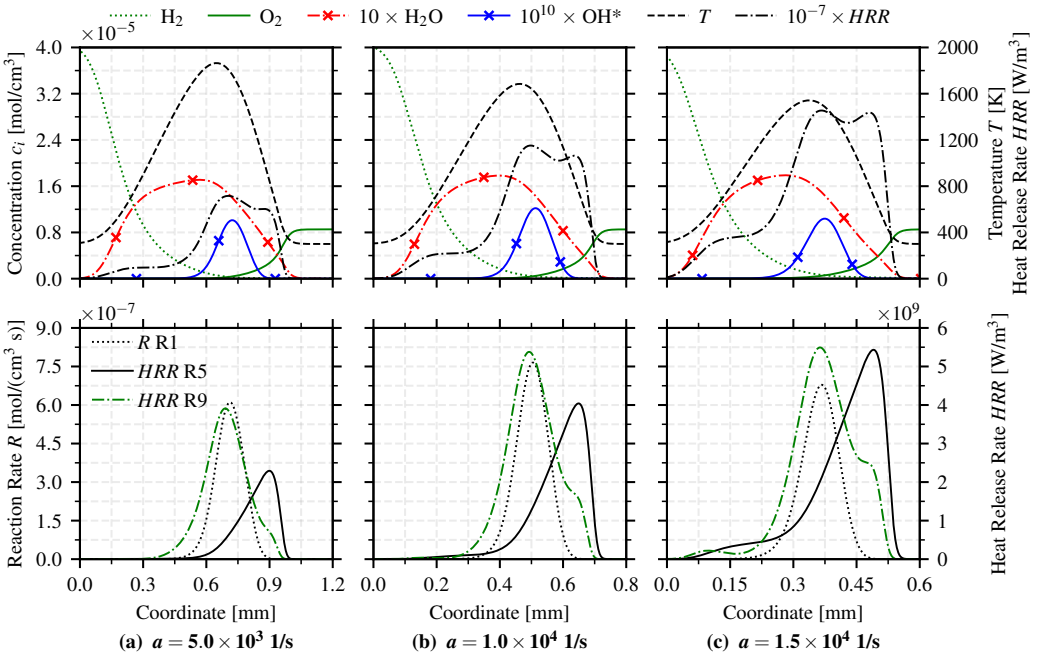

Fig. 4: Structure of hydrogen-air diffusion flames at T_u = 300 K and p = 1 atm for a strain rate a equal to $5.0{\times}10^3$ s^{-1} (a), $1.0{\times}10^4$ s^{-1} (b) and $1.5{\times}10^4$ s^{-1} (c). Molar concentrations of fuel and oxidizer, temperature and heat release rate profiles (top), chemical rates and heat release rates of selected reactions (bottom).

the oxidizer side. A similar behavior has been found for methane inverse diffusion flames [30]. Differently from the premixed configuration, in H_2-air diffusion flames HRR is dominated, on the fuel side, by the following reaction:

$$\mathrm{H + OH + M \rightleftharpoons H_2O + M} \qquad \text{(R9)}$$

which needs the production of H-radicals on the hydrogen fuel side. Reaction (R5), discussed for premixed flames in Section 3.1, requires instead O_2 and, therefore, peaks on the oxidizer side [28].

At low and moderate strain rates (Figs. 4a-b) reaction (R9) (dash-dotted green line) prevails on reaction (R5) (solid black line). Since reaction (R1) (dotted black line) requires the H-radical, its reaction rate and so the OH* concentration (cross-marked solid blue line) well correlate with reaction (R9). Therefore, OH* well behaves as HRR global peak tracer, differently than in premixed flames.

Marshall and Pitz [5] studied lean premixed cellular tubular flames at two different stretch rates and found that increasing stretch slightly improves the OH*-HRR correlation. In contrast with [5], increasing the strain rate here appears to weaken the OH*-HRR correlation. Indeed, for higher strain rates (Fig. 4c) the heat released by reaction (R5) increases, and so does the magnitude of $\mathrm{HRR}^{\mathrm{O}}_{\mathrm{max}}$, which eventually overtakes $\mathrm{HRR}^{\mathrm{F}}_{\mathrm{max}}$. Since OH* does not follow the bimodal nature of HRR and, as in premixed flames, does not correlate well with (R5), a shift between OH* peak and the HRR global maximum appears. Still, as these regimes are close to extinction (the extinction strain rate being $\sim 1.8{\times}10^4$ s^{-1}), they are not of interest for practical applications.

3.3. Quantitative analysis

The differences between premixed and diffusion flames when switching from CH_4 to CH_4-H_2 blends and, finally, to pure H_2 have been characterized qualitatively. To allow for a direct comparison between different cases, it is of interest to define a numerical parameter to quantify the OH*-HRR correlation.

Nikolau and Swaminathan [4] proposed an error estimator method to determine the reliability of HRR markers for premixed combustion of carbon-based fuels. This method is based on the evaluation of an error measure $\zeta(v)$ for a variable v, where a lower value of $\zeta(v)$ indicates a better correlation of v with HRR. The definition of $\zeta(v)$ proposed in [4], however, is well posed for unstrained premixed flames only and strongly depends on the overall dimension of the computational domain, hindering the comparison of different flame configurations. Therefore, a modified definition is adopted here:

$$\bar{\zeta}(v) = \frac{1}{L_r}\int_{reac} (|HRR(x)|_{norm} - |v(x)|_{norm})^2\, dx \qquad (1)$$

The error measure $\bar{\zeta}(v)$ is the mean of $\zeta(v)$ over the reactive region of size L_r, here defined by the condition $|HRR(x)| \geq 0.01\max(|HRR(x)|)$. As in [4], $|HRR(x)|$ and $|v(x)|$ are normalized by their respective maxima.

Table 3 reports the values of $\bar{\zeta}$ computed for OH* in the premixed and diffusion flames shown in Figs. 3 and 4, respectively. The products of the concentrations of O_2 and H, which react in reaction (R5),

Table 3: Error measure $\bar{\zeta}$ computed for different variables in premixed and diffusion flames.

Case	Molar concentrations				Chemical rates		Heat release rates		
	OH^*	$O_2 \times H$	$OH \times H_2$	HCO	R1	R4	R5	R6	R9
Premixed Flames (ϕ = 1)									
CH_4 (Fig. 3a)	1.45E-02	1.06E-01	4.46E-01	1.43E-03	2.62E-01	1.50E-02	9.81E-02	4.69E-03	2.84E-01
$CH_4 + H_2$ (Fig. 3b)	1.22E-02	4.49E-02	3.62E-01	3.11E-03	2.16E-01	1.32E-02	3.79E-02	5.32E-03	2.17E-01
H_2 (Fig. 3c)	5.89E-02	1.07E-02	2.78E-02	-	5.50E-02	-	1.85E-02	-	3.53E-02
Diffusion Flames									
a = 5.0E+03 (Fig. 4a)	1.11E-01	8.71E-02	1.36E-01	-	1.12E-01	-	1.20E-01	-	5.99E-02
a = 1.0E+04 (Fig. 4b)	1.45E-01	8.77E-02	1.35E-01	-	1.46E-01	-	1.13E-01	-	6.68E-02
a = 1.5E+04 (Fig. 4c)	1.73E-01	8.10E-02	1.20E-01	-	1.74E-01	-	9.65E-02	-	6.43E-02

and of OH and H_2, identified as the most adequate HRR marker for H_2-air flames in [5], are also considered, together with HCO for CH_4 and CH_4-H_2 flames. The chemical rates of reactions (R1) and (R4), and the heat release rates of reactions (R5), (R6) and (R9) are included too. The premixed cases show that for CH_4 and CH_4-H_2 flames, as expected, the lowest values of the error measure are obtained for HCO and for the reaction (R6) by which it is produced. For these flames, the value of $\bar{\zeta}(OH^*)$ is close to the one of $\bar{\zeta}$(R4) and lower than $\bar{\zeta}$(R1) by one order of magnitude. This confirms that, when CH_4 is present, H_2 has a limited impact on the OH^* chemical pathway via reaction (R4), as discussed in Section 3.1. For pure H_2 flames, the value of $\bar{\zeta}(OH^*)$ is the largest, confirming a worse correlation between OH^* and HRR for these flames. Here, the lowest values are obtained for the $O_2 \times H$ product and for reaction (R5), coherently with the analysis of the flame structures in Fig. 3c. The product of OH and H_2 concentrations shows also a low value, in agreement with [5]. Overall, no variable reaches a value of $\bar{\zeta}$ as low as $\bar{\zeta}$(HCO) in CH_4 and CH_4-H_2 flames, indicating that a reliable HRR marker is harder to define for pure H_2-air flames. As for H_2-air diffusion flames, the values of $\bar{\zeta}$ are higher than in the premixed case and the variability among different quantities is less pronounced. Indeed, the bimodal nature of the HRR distribution introduces a bias in the evaluation of $\bar{\zeta}$ because none of the variables can reproduce it. The OH^* and the reaction (R1) by which it is produced, as well as reaction (R9) and the product $OH \times H_2$, peak on the fuel side, while reaction (R5) and the product of its reactants O_2 and H peak on the oxidizer side. Coherently with Section 3.2, the value of $\bar{\zeta}(OH^*)$ increases with the strain rate, suggesting a worse correlation of OH^* with HRR. Nevertheless, the dependency of $\bar{\zeta}$ on strain rate is quite limited for all variables, since the normalization of the integrands in Eq. (1) cancels out the variation of the relative magnitude of variables shown in Fig. 4. The sole error measure is thus insufficient to assess the adequacy of a HRR marker for these flames.

4. Turbulent three-dimensional flames

Large Eddy Simulations (LES) predictions of the OH^* field in turbulent hydrogen-air flames are here discussed to assess the conclusions for premixed and diffusion one-dimensional flames in a turbulent swirling flow configuration and validate them against experimental data. The reference configuration is the HYLON injector from IMFT (Fig. 5a), which consists of two swirling coaxial ducts to separately inject hydrogen and oxidizer [14]. At the outlet section of the injector, turbulent mixing competes with the chemical times of H_2-air flames, leading to the stabilization of either an anchored diffusion flame (denoted as Flame A in Fig. 5b) or of a lifted partially premixed flame (Flame L in Fig. 5c). The global equivalence ratio is kept constant to $\phi_g = 0.45$ for both flames.

The same numerical methodology and computational mesh described in [14] are employed. Only key features are recalled hereafter. Simulations are performed with the compressible LES solver AVBP (www.cerfacs.fr/avbp7x). Flame-turbulence interaction for premixed flames is addressed with the DTFLES model, while a sufficient mesh refinement is imposed to avoid flame thickening in zones of stabilized diffusion flames. Inlet and outlet boundary conditions are treated with the NSCBC formalism and a thermal resistance is imposed to account for wall heat losses. Solutions are time-averaged over a whole flow-through time, corresponding to approximately 55 ms for Flame A and 25 ms for Flame L.

In addition to the results in [14], the Kathrotia OH^* sub-mechanism [12] is here included in the San Diego skeletal scheme [26]. Thus, Fig. 6 compares the experimental images of the mean normalized OH^*_{norm} chemiluminescence signal with LES normalized time-averaged OH^*_{norm} fields. Contours at 90%, 50% and 20% of OH^*_{norm} (white lines) and HRR_{norm} (red lines) are superimposed to the latter. Being controlled by diffusion reaction, the attached flame (Fig. 6a) shows a good match between numerical OH^*_{norm} and HRR_{norm} fields. This is in agreement with the laminar counterflow flame simulations for moderate strain rates. For the lifted flame (Fig. 6b), instead, albeit the flame shape is globally well predicted, slight differences on the axial extension of the experimental OH^*_{norm} and numerical HRR_{norm} fields are observed (as noted also in Fig. 13 in [14]). A better match is achieved when the experimental and LES time-averaged OH^*_{norm} fields are directly compared, as highlighted by horizontal dashed lines. The Flame L, burning in the partially premixed regime, features a shift between HRR_{norm} and OH^*_{norm} peaks, as observed

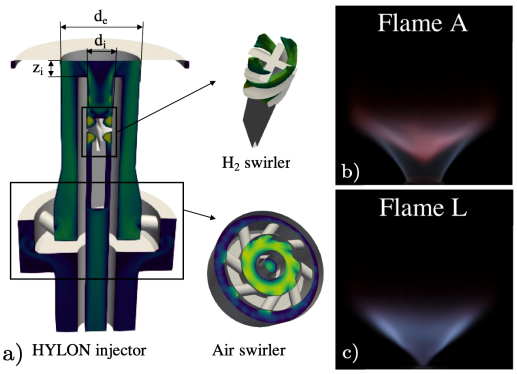

Fig. 5: HYLON injector main components (a), and line-of-sight integrated images of attached (b, Flame A) and lifted (c, Flame L) flames [14].

in Section 3.1 for canonical premixed flames.

5. Conclusion

In this work, the OH* distribution and its relation with HRR in laminar and turbulent hydrogen-air flames have been studied. First, in laminar premixed one-dimensional hydrogen-air flames, OH* has been found not to adequately mark the position of maximum HRR. A shift between the two peaks has been observed irrespective of the equivalence ratio or OH* kinetics sub-mechanism. For fuel mixtures containing methane, instead, a good correlation between OH* and HRR has been retrieved. To understand the mechanisms at the origin of these differences, flame structures have been analyzed, emphasizing the pivotal role of the H-radical and, in particular, of its part in the main reaction pathways leading to OH* formation and HRR. The chain-branching nature of hydrogen-air flames has been found to enhance the H-radical pool in the post-flame region leading to OH* formation. HRR has been found to peak further upstream than OH*, being linked to the HO_2-radical generated by the recombination reactions of back-diffused H-radical. A chain-terminating behavior has been observed, instead, for methane and methane-hydrogen flames, where methane consumes H, generating HRR and preventing the radical pool formation in the post-flame zone, thus leading to different OH* formation pathways linked to CH.

A different behavior has been observed for laminar strained counterflow diffusion flames, where OH* has been shown to be a more adequate HRR marker at strain rates far from extinction. Indeed, differently from premixed flames, HRR is in this case dominated by the direct consumption of the H-radical on the fuel side. At higher strains, reactions based on the HO_2-radical have been observed to become more important, leading to a shift in the HRR global maximum not followed by OH*. Still, being close to the extinction strain rate, this has limited practical interest.

Finally, the capabilities of OH* numerical predictions to well represent experimental findings have been investigated via LES of attached and lifted turbulent hydrogen-air flames stabilized through the HYLON injector. In agreement with the observations made for laminar one-dimensional flames, a good match has been observed for the diffusion flame branch between the LES-computed time-averaged HRR_{norm} and the experimental mean OH^*_{norm} Abel-deconvoluted chemiluminescence signals. For the lifted partially premixed flame branch, instead, LES has shown a slight downward axial shift. In this case, a better agreement has been found between experimental and numerical OH^*_{norm} fields, highlighting the importance of adding a OH* sub-scheme to directly compare LES of non-diffusion hydrogen-air flames with experiments. In future work, the same methodology could be extended to investigate turbulent ultra-lean hydrogen-air flames at high pressure and temperature operating conditions.

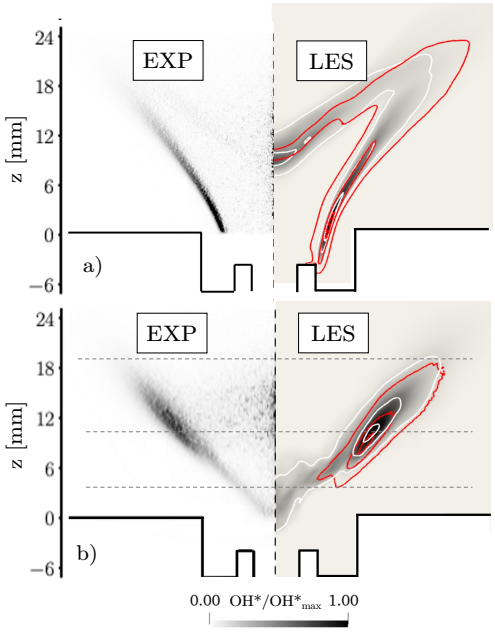

Fig. 6: Experimental normalized mean OH^*_{norm} Abel-deconvoluted chemiluminescence signal (left) and LES normalized time-averaged OH^*_{norm} mass fraction (right) for Flame A (a) and Flame L (b), with iso-lines at 90%, 50% and 20% of OH^*_{norm} (white lines) and HRR_{norm} (red lines).

Declaration of competing interest

The authors declare that they have no known competing financial interests or personal relationships that could have appeared to influence the work reported in this paper.

Acknowledgments

This work was supported by the Italian Min-

istry of University and Research under the National Recovery and Resilience Plan (NRRP) funded by the European Union - NextGenerationEU with the grant CUP – D93C22000410001 (National Sustainable Mobility Center – MOST, Spoke 14 "Hydrogen and New Fuels") and by the French "Agence Nationale de la Recherche (ANR)" under the grant ANR-22-CE50-0024-1 (TOHREAU). HPC resources from PRACE project 2021240098 (WONDER) and EuroHPC project EHPC-REG-2023R03-184 (PROMETH2EUS) are highly acknowledged.

Supplementary material

Supplementary material is submitted along with the manuscript.

References

[1] A. Gazi, G. Vourliotakis, G. Skevis, M. A. Founti, Assessment of chemical markers for heat-release rate correlations in laminar premixed flames, Combust. Sci. Technol. 185 (10) (2013) 1482–1508.

[2] M. Lauer, T. Sattelmayer, On the adequacy of chemiluminescence as a measure for heat release in turbulent flames with mixture gradients, ASME J. Eng. Gas Turbines Power 132 (6) (2010) 061502.

[3] H. N. Najm, P. H. Paul, C. J. Mueller, P. S. Wyckoff, On the Adequacy of Certain Experimental Observables as Measurements of Flame Burning Rate, Combust. Flame 113 (3) (1998) 312–332.

[4] Z. M. Nikolaou, N. Swaminathan, Heat release rate markers for premixed combustion, Combust. Flame 161 (12) (2014) 3073–3084.

[5] G. J. Marshall, R. W. Pitz, Evaluation of heat release indicators in lean premixed H2/Air cellular tubular flames, Proc. Combust. Inst. 37 (2019) 2029–2036.

[6] Y. Ding, D. Durox, N. Darabiha, T. Schuller, Chemiluminescence of burner-stabilized premixed laminar flames, Combust. Sci. Technol. 191 (1) (2019) 18–42.

[7] C. Panoutsos, Y. Hardalupas, A. Taylor, Numerical evaluation of equivalence ratio measurement using OH* and CH* chemiluminescence in premixed and non-premixed methane–air flames, Combust. Flame 156 (2) (2009) 273–291.

[8] Y. Hu, J. Tan, L. Lv, X. Li, Investigations on quantitative measurement of heat release rate using chemiluminescence in premixed methane-air flames, Acta Astronaut. 164 (2019) 277–286.

[9] M. Reyes, F. Tinaut, B. Giménez, J. V. Pastor, Effect of hydrogen addition on the OH* and CH* chemiluminescence emissions of premixed combustion of methane-air mixtures, Int. J. Hydrogen Energy 43 (42) (2018) 19778–19791.

[10] R. W. Schefer, W. D. Kulatilaka, B. D. Patterson, T. B. Settersten, Visible emission of hydrogen flames, Combust. Flame 156 (6) (2009) 1234–1241.

[11] S. Yoo, C. K. Law, S. Tse, Chemiluminescent OH* and CH* flame structure and aerodynamic scaling of weakly buoyant, nearly spherical diffusion flames, Proc. Combust. Inst. 29 (2002) 1663–1670.

[12] T. Kathrotia, M. Fikri, M. Bozkurt, M. Hartmann, U. Riedel, C. Schulz, Study of the H + O + M reaction forming OH*: Kinetics of OH* chemiluminescence in hydrogen combustion systems, Combust. Flame 157 (7) (2010) 1261–1273.

[13] A. A. Konnov, On the role of excited species in hydrogen combustion, Combust. Flame 162 (10) (2015) 3755–3772.

[14] A. Aniello, D. Laera, S. Marragou, H. Magnes, L. Selle, T. Schuller, T. Poinsot, Experimental and numerical investigation of two flame stabilization regimes observed in a dual swirl H2-air coaxial injector, Combust. Flame 249 (2023) 112595.

[15] M. Zhao, D. Buttsworth, R. Choudhury, Experimental and numerical study of OH* chemiluminescence in hydrogen diffusion flames, Combust. Flame 197 (2018) 369–377.

[16] Y. Hidaka, S. Takahashi, H. Kawano, M. Suga, W. C. Gardiner Jr., Shock-tube measurement of the rate constant for excited hydroxyl(A2.SIGMA.+) formation in the hydrogen-oxygen reaction, J. Phys. Chem. 86 (8) (1982) 1429–1433.

[17] T. Kathrotia, U. Riedel, A. Seipel, K. Moshammer, A. Brockhinke, Experimental and numerical study of chemiluminescent species in low-pressure flames, Appl. Phys. B 107 (3) (2012) 571–584.

[18] C. I. Heghes, C1-C4 Hydrocarbon Oxidation Mechanism, Ph.D. Thesis, Ruprecht Karl University of Heidelberg, Heidelberg, Germany (2007).

[19] J. Graña-Otero, S. Mahmoudi, Excited OH kinetics and distribution in H2 premixed flames, Fuel 255 (2019) 115750.

[20] D. G. Goodwin, H. K. Moffat, R. L. Speth, Cantera: An Object-oriented Software Toolkit for Chemical Kinetics, Thermodynamics, and Transport Processes. Version 2.3.0 (2017).

[21] G. Dixon-Lewis, Flame structure and flame reaction kinetics II. Transport phenomena in multicomponent systems, Proc. R. Soc. London, Ser. A 307 (1488) (1968) 111–135.

[22] J. F. Grcar, J. B. Bell, M. S. Day, The Soret effect in naturally propagating, premixed, lean, hydrogen–air flames, Proc. Combust. Inst. 32 (2009) 1173–1180.

[23] P. Saxena, F. A. Williams, Testing a small detailed chemical-kinetic mechanism for the combustion of hydrogen and carbon monoxide, Combust. Flame 145 (1-2) (2006) 316–323.

[24] E. Ranzi, A. Frassoldati, A. Stagni, M. Pelucchi, A. Cuoci, T. Faravelli, Reduced kinetic schemes of complex reaction systems: fossil and biomass-derived transportation fuels, Int. J. Chem. Kinet. 46 (9) (2014) 512–542.

[25] P. E. Lapenna, L. Berger, F. Creta, H. Pitsch, in: E.-A. Tingas (Ed.), Hydrogen for Future Thermal Engines, Springer, Cham, Switzerland, 2023, pp. 93–139.

[26] A. L. Sánchez, F. A. Williams, Recent advances in understanding of flammability characteristics of hydrogen, Prog. Energy Combust. Sci. 41 (2014) 1–55.

[27] F. A. Williams, Progress in knowledge of flamelet structure and extinction, Prog. Energy Combust. Sci. 26 (4-6) (2000) 657–682.

[28] C. K. Law, Combustion Physics, Cambridge University Press, Cambridge, UK, 2006, pp. 284–301.

[29] K. Seshadri, Multistep asymptotic analyses of flame structures, Proc. Combust. Inst. 26 (1996) 831–846.

[30] S. Yan, Y. Gong, Z. Duan, Q. Guo, G. Yu, Investigation of the correlation between OH*, CH* chemiluminescence and heat release rate in methane inverse diffusion flame, Energy 283 (2023) 129162.